



## **As-Built and Post-treated Microstructures of an Electron Beam Melting (EBM) Produced Nickel-Based Superalloy**

Downloaded from: <https://research.chalmers.se>, 2024-03-13 08:59 UTC

Citation for the original published paper (version of record):

Goel, S., Mehtani, H., Yao, S. et al (2020). As-Built and Post-treated Microstructures of an Electron Beam Melting (EBM) Produced Nickel-Based Superalloy. Metallurgical and Materials Transactions A: Physical Metallurgy and Materials Science, 51(12): 6546-6559. <http://dx.doi.org/10.1007/s11661-020-06037-z>

N.B. When citing this work, cite the original published paper.

# As-Built and Post-treated Microstructures of an Electron Beam Melting (EBM) Produced Nickel-Based Superalloy



SNEHA GOEL, HITESH MEHTANI, SHU-WEI YAO, INDRADEV SAMAJDAR, UTA KLEMENT, and SHRIKANT JOSHI

The microstructures of an electron beam melted (EBM) nickel-based superalloy (Alloy 718) were comprehensively investigated in as-built and post-treated conditions, with particular focus individually on the contour (outer periphery) and hatch (core) regions of the build. The hatch region exhibited columnar grains with strong  $\langle 001 \rangle$  texture in the build direction, while the contour region had a mix of columnar and equiaxed grains, with no preferred crystallographic texture. Both regions exhibited nearly identical hardness and carbide content. However, the contour region showed a higher number density of fine carbides compared to the hatch. The as-built material was subjected to two distinct post-treatments: (1) hot isostatic pressing (HIP) and (2) HIP plus heat treatment (HIP + HT), with the latter carried out as a single cycle inside the HIP vessel. Both post-treatments resulted in nearly an order of magnitude decrease in defect content in hatch and contour regions. HIP + HT led to grain coarsening in the contour, but did not alter the microstructure in the hatch region. Different factors that may be responsible for grain growth, such as grain size, grain orientation, grain boundary curvature and secondary phase particles, are discussed. The differences in carbide sizes in the hatch and contour regions appeared to decrease after post-treatment. After HIP + HT, similar higher hardness was observed in both the hatch and contour regions compared to the as-built material.

<https://doi.org/10.1007/s11661-020-06037-z>  
© The Author(s) 2020

## I. INTRODUCTION

ADDITIVE manufacturing (AM), commonly known as 3D printing, is a rapidly growing group of processing technologies comprehensively reviewed by Horn and Harrysson.<sup>[1]</sup> In AM, it is possible to produce geometrically complex components directly from computer-aided design (CAD) models.<sup>[2]</sup> The ease of manufacturing, compared to the traditional production routes, makes AM a promising emerging technology. Electron beam melting (EBM) and laser powder bed fusion (LPBF) are two commonly used AM technologies

based on powder bed fusion, as broadly reviewed by Frazier.<sup>[3]</sup> EBM makes use of a high-energy electron beam to selectively melt and consolidate appropriate regions of each layer of powder raked to build a component in layer-by-layer fashion.<sup>[4]</sup> EBM processing of nickel-based superalloys (example: Alloy 718) appears particularly promising to the aircraft engine industry,<sup>[5]</sup> which demands complex parts manufactured from difficult-to-machine materials. During EBM processing, individual layers undergo various processing steps, with the typical melting steps involving contour and hatch scanning as detailed in Reference 6. For every layer, the perimeter of the component(s), also known as contour, is typically melted by a ‘multi-spot’ melting strategy. During this step, the spot melting pattern is used to create a ‘frame’ of the component according to a pre-defined CAD geometry as elaborated in Reference 7. This step is followed by hatch melting, during which the beam typically scans in a raster pattern to consolidate the region(s) contained within the contour(s). In a word, the hatch melting melts the bulk material while the contour scanning provides adherence to component geometry.<sup>[8]</sup> The thickness of the contour region is thus fixed, but the extent of the hatch region depends on the overall component dimensions.<sup>[9]</sup> In case of thinner

---

SNEHA GOEL and SHRIKANT JOSHI are with the Department of Engineering Science, University West, 461 86 Trollhättan, Sweden. Contact e-mail: sneha.goel@hv.se HITESH MEHTANI and INDRADEV SAMAJDAR are with the Department of Metallurgical Engineering and Materials Science, Indian Institute of Technology Bombay, Mumbai, 400076 India. SHU-WEI YAO is with the School of Materials Science and Engineering, Xi'an Jiaotong University, Xi'an, 710049 China. UTA KLEMENT is with the Department of Industrial and Materials Science, Chalmers University of Technology, 412 96 Göteborg, Sweden.

Manuscript submitted February 22, 2020; accepted September 17, 2020.

Article published online October 18, 2020

sections, the microstructure of the contour thus becomes critical. It is worth mentioning that the order of contour and hatch scanning can be modified, and typically for EBM manufacturing of Alloy 718, the contour is melted before the hatch.

Alloy 718 is a precipitation-hardened Ni-based superalloy, which is used in varied operating environments, such as for high temperature as well as cryogenic applications in diverse fields such as aerospace, oil and gas, nuclear industries, *etc.* Such extensive usage is attributed to its high strength and excellent corrosion resistance combined with good weldability, creep and fatigue properties.<sup>[10]</sup> Alloy 718 derives strength mainly by the coherent metastable  $\gamma''$ (Ni<sub>3</sub>Nb) and  $\gamma'$ (Ni<sub>3</sub>(Al,Ti)) precipitates present in the  $\gamma$ -FCC matrix. Other phases present in Alloy 718 impart additional properties. For instance, the thermodynamically stable  $\delta$  phase (Ni<sub>3</sub>Nb) present at the grain boundaries is known to control grain size during heat treatment and thermo-mechanical working. While the  $\gamma''$ ,  $\gamma'$  and  $\delta$  phases precipitate during solid-state transformation, the primary carbides form during solidification as stated in the solidification path proposed by Knorovsky *et al.*<sup>[11]</sup> based on the differential thermal analysis. The MC-type primary carbides ( $M$  = Nb, Ti) are also known to pin grain boundaries at high temperatures as observed by Kirka *et al.*,<sup>[12]</sup> who attributed the lack of grain growth after hot isostatic pressing (HIP) (at 1200 °C) of EBM Alloy 718 to Zener pinning by these carbides present at the grain boundaries. The precipitation of  $\gamma''$ ,  $\delta$ , primary NbC carbides is related mainly to the Nb segregation, Nb being a key alloying element in Alloy 718. During solidification, Nb segregates in the interdendritic regions because of its larger atomic radius.<sup>[13]</sup> The degree of segregation depends on the solidification parameters, such as the cooling rate. Zhang *et al.*<sup>[14]</sup> simulated the cooling rates for Alloy 718 during LBPf and casting and found it to be significantly higher in the former ( $10^3$  to  $10^6$  K/s) compared to the latter (3.8 K/s). In EBM Alloy 718, prior work by Kirka *et al.*<sup>[15]</sup> has experimentally approximated (through primary dendrite arm spacing) the cooling rate to be  $10^3$  K/s. In this context it is worth mentioning that, in cast alloy 718, both Mitchell<sup>[16]</sup> and Patel *et al.*<sup>[17]</sup> have observed that an increase in cooling rate caused a decrease in carbide size.

There have been significant research efforts on EBM processing of Alloy 718, such as tailoring the grain structure through both experiments and modeling by Helmer *et al.*,<sup>[18]</sup> Raghavan *et al.*,<sup>[19]</sup> Balachandramurthi *et al.*<sup>[20]</sup> and others. For instance, Helmer *et al.*<sup>[18]</sup> have shown that the microstructure in the EBM-built Alloy 718 can be tailored by changing the scanning strategy and thus the thermal gradient during solidification. If the thermal gradient is aligned in the preferred direction, columnar grains grow; otherwise, equiaxed grains can form. Raghavan *et al.*<sup>[19]</sup> found that the preheating temperature (one of the indirect control parameters in the Arcam process) has a significant effect on the volume fraction of the formed equiaxed grains. Balachandramurthi *et al.*<sup>[20]</sup> have shown that for the ‘multi-spot’ melting strategy the microstructure is affected by the relationship among processing parameters, melting

patterns and part geometry and also by the control of energy input. Such increased understanding of the process-structure correlation has not been complemented by understanding the influence of thermal post-treatments on the microstructure. The latter can potentially suppress the inevitable defects (gas porosity, shrinkage porosity and lack-of-fusion), undesirable micro-segregation, *etc.*, present in the microstructure. The commonly applied post-treatments include HIP and heat treatment (HT). The latter typically involves solution treatment and aging. The majority of past research efforts on the application of post-treatments focused on the hatch region of EBM Alloy 718 as previously detailed by Deng *et al.*,<sup>[21]</sup> Nandwana *et al.*<sup>[22]</sup> and others. The hatch region typically consists of elongated columnar  $\gamma$  grains having strong  $\langle 001 \rangle$  texture in the build direction. The contour region, on the other hand, usually exhibits a mix of fine equiaxed grains, curved thin columnar grains and wide columnar grains.<sup>[21]</sup> Deng *et al.*<sup>[21]</sup> attributed the observed difference in the grain structures of the hatch vs. contour regions to the different melting strategies. Given the significant differences in the microstructure, there is a need for investigating the effect of post-treatments, between these regions, of the EBM-built Alloy 718. This has been an important motivation behind this study. Although prior work by the authors has involved investigation of aspects related to uniformity in a typical EBM Alloy 718 build,<sup>[23]</sup> inclusions and precipitates in as-built and post-treated material,<sup>[24]</sup> extent of defect closure during HIPing in builds with intentionally introduced defects,<sup>[25]</sup> *etc.*, the response of hatch and contour regions to identical post-treatments remains not fully investigated.

In the present study, detailed microstructural analysis of EBM-built Alloy 718 was carried out and followed with different post-treatment cycles. The two post-treatments carried out were: HIP and HIP + HT. The latter involved solution treatment and two-step aging preceded by HIP and was carried out as a single cycle inside the HIP vessel. The texture, grain morphology and grain size were comprehensively investigated using scanning electron microscopy (SEM) and electron backscattered diffraction (EBSD). Moreover, the defects, carbides,  $\delta$  phase and  $\gamma''/\gamma'$  phases in the material and the micro-hardness were investigated.

## II. EXPERIMENTAL PROCEDURE

### A. EBM Manufacturing of Alloy 718

Plasma wire atomized Alloy 718 powder used in the current study was supplied by AP&C (Quebec, Canada). This powder had a nominal size range of 45 to 106  $\mu\text{m}$ , and its chemical composition is given in Table I. An A2X EBM machine (Arcam AB, Sweden) was used for the production of Alloy 718 specimens. Two builds were produced using the recommended EBM process parameter settings (process theme 4.1.22 and EBMC 4.1) as stated in a previous study by Goel *et al.*<sup>[24]</sup> The following specimens were manufactured: (1) rods (100  $\times$  15 mm)

**Table I. Nominal Chemical Composition of the Starting Powder in Wt Pct**

Element	Ni	Cr	Fe	Nb	Mo	Ti	Al	C	N	Ta
Alloy 718	51.67	19.09	bal.	5.31	3.12	0.89	0.53	0.04	0.02	< 0.01

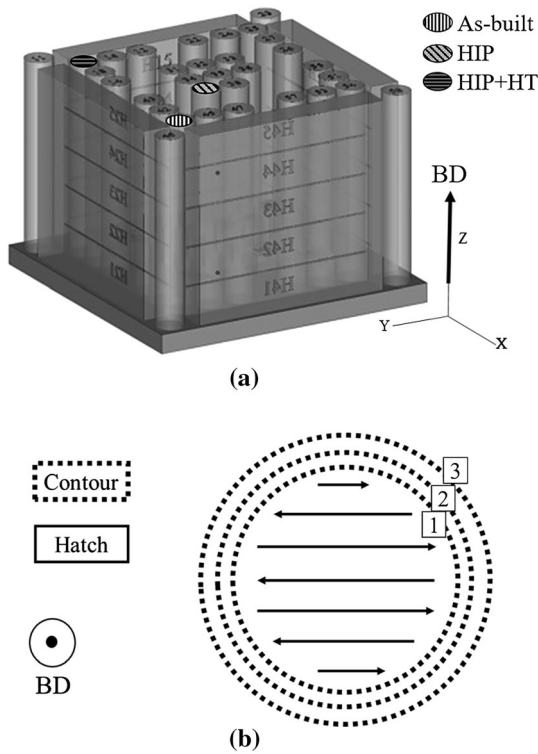


Fig. 1—(a) CAD geometry of the investigated EBM build comprising rods and cuboids. The specimens characterized in the as-built and post-treated conditions are marked. (b) Simplified schematic showing contour and hatch melting strategies for specimens with a circular cross-section, where ‘multi-spot’ melting was employed for contour and bidirectional raster scanning was used for hatch. The arrow and the encircled dot indicate the build direction.

oriented along the build direction [CAD geometry of the build is given in Figures 1(a) and (b) flat specimens (5 × 19 mm)]. The processing cycle for each layer consisted of six steps: (1) pre-heating of the powder layer being processed, (2) localized pre-heating in the regions to be melted, (3) contour-melting of the perimeter of the specimens, (4) hatch-melting of the region enclosed by the contours, (5) localized post-heating in the melted regions and (6) lowering of powder bed by 75  $\mu\text{m}$  and raking of powder to form a uniform layer for the next cycle. While the details related to melting are described below, it should be mentioned that the preheating was done to sinter the powder particles using a beam current of 48 mA, and the post-heating was carried out based on the automatic power calculation in the EBM machine.

The melting strategy used for contour and hatch were ‘multi-spot’ and bi-directional raster scanning, respectively. Karlsson *et al.*<sup>[7]</sup> have previously elaborated these

melting strategies. Figure 1(b) shows a simplified schematic of the used melting strategies. As can be observed from the schematic, the contour region was consolidated by three passes, numbered as 1, 2 and 3. These passes were applied in ascending order; therefore, contour melting started with pass 1, then pass 2 and ended with pass 3. All the contour passes were processed with the same default parameters. Thereafter, hatch melting was applied. For every added layer, the scanning direction for the hatch region was rotated by 72 deg. Prior to the start of the process, the stainless-steel build plate was preheated to 1025 °C. The acceleration voltage and hatch spacing (distance between any two consecutive scanning lines) were set to 60 kV and 125  $\mu\text{m}$ , respectively.

## B. Post-treatments

Some of the rods and flat specimens were exposed to two different post-treatments, one consisting of HIP only and another including HIP and heat treatment (HIP + HT). HIP + HT combined in a single cycle inside the HIP vessel. The details of the temperature-time-pressure applied during the two post-treatments were as follows: (1) HIP: 1200 °C for 4 hours at 120 MPa, rapidly cooled to room temperature; (2) HIP + HT: 1185 °C for 3 hours at 170 MPa, followed by cooling to solution treatment temperature of 980 °C and 1 hours holding at 157 MPa, succeeded by rapid cooling to room temperature. Thereafter, the first age hardening was carried out by heating to 740 °C and holding for 8 hours at 138 MPa, furnace cooling to 635 °C for second age-hardening and holding for 10 hours at 131 MPa, and then quenching to room temperature. Argon was used as the inert process gas. Unlike HIP + HT, the HIP treatment was carried out at constant pressure of 120 MPa, which can be seen from the process graphs previously given in Reference 24. HIPing parameters were chosen based on the previously published research on mechanical property evaluation of the EBM-built Alloy 718.<sup>[12]</sup> It may be noted that the HIPing conditions for the HIP and the HIP + HT (as stated above) were different. Given the high processing cost in an industrial large-volume HIP furnace, a pre-planned client run for AM-built Alloy 718 was used for this one of the first reported research on combined post-treatment of Alloy 718. In this regard, it is worth mentioning that previously reported studies on HIPing of Alloy 718 have shown that a decrease in duration from 4 to 3 hours<sup>[26]</sup> and increase in pressure by 50 MPa<sup>[27]</sup> led to only modest change in the number of defects. Therefore, the temperature-time-pressure schedule used herein was considered reasonable.



### C. Materials Characterization

For microstructural investigation, sections along and perpendicular (henceforth referred as transverse direction) to the build direction were taken from the middle of the length of the as-built and post-treated rod specimens. Sectioning was performed by employing precision cutting with an alumina blade, and the extracted specimens were hot mounted. Samples were semi-automatically polished using the Buehler PowerPro 5000 (Buehler) system. The polished specimens were etched *via* electrolytic etching (2 to 4 V, 3 to 10 seconds) using oxalic acid and Kallings' 2 reagent (50 pct diluted with ethanol) and were then examined under an optical microscope (OM) (Olympus<sup>TM</sup> BX60M, HOFSTRAGroup<sup>®</sup>) and two SEMs (Hitachi<sup>TM</sup> TM3000, Zeiss<sup>TM</sup> 1550 Gemini equipped with an HKL Nordlys EBSD detector). Image analysis was employed for quantification of defects and carbide content (using the ASTM E1245-03<sup>[28]</sup> automatic image analysis method and the open source ImageJ software), and the average value  $\pm 95$  pct confidence interval has been reported as recommended in the above-mentioned ASTM standard. It should be mentioned that, for defect quantification, the samples were analyzed prior to etching to avoid etching artifacts. Defect and carbide analyses were done using ten image fields. For image analysis, recognizing the threshold can influence the results; therefore, for each analysis, a similar threshold was used across different samples.

For detailed EBSD analysis of flat specimens, the as-built and post-treated flat specimens were sectioned only along the build direction. The samples were metallographically prepared and electropolished in an electrolyte of 80:20 (methanol:perchloric acid), 20 V DC and  $-20$  °C. Measurements were made on a Fei<sup>TM</sup> Nova Nano SEM with an EDAX<sup>TM</sup> EBSD + EDS (energy dispersive X-ray spectroscopy) system. The EBSD data were processed to obtain the orientation maps, kernel average misorientation (KAM), grain average misorientation (GAM) and grain orientation spread (GOS). Average misorientation between any pixel point and its immediate neighbors (six in the present case using a hexagonal grid) was considered as KAM, provided any of these misorientation did not exceed 5 deg. KAM, calculated for the  $i$ th pixel, was defined as<sup>[29]</sup>:

$$\text{KAM}_i = \frac{1}{6} \sum_j (g_i - g_j) \quad [1]$$

where  $g_i$  represents the misorientation between the  $i$ th pixel and its neighboring points ( $g_j$ ). For estimates of GAM or GOS, a grain definition was essential. A grain was defined as a region bound by  $\geq 5$  deg continuous boundary. GAM represented the average misorientation between each measurement point in such grains and was evaluated as follows<sup>[29]</sup>:

$$\text{GAM} = \frac{1}{N} \sum_{i=1}^N \left[ \sum_{j=1}^{nm} (g_i g_j^{-1}) \right] \quad [2]$$

For estimating GOS, the average (quaternion average) grain orientation was calculated. Misorientation between the average orientation and all measurement points within the grain provided the GOS value. GOS, calculated for each grain, was defined as<sup>[29]</sup>:

$$\text{GOS} = \frac{1}{N} \sum_{i=1}^N (g_{av} g_i^{-1}) \quad [3]$$

where  $g_{av}$  is the quaternion average of the grain orientation. Vickers micro-hardness testing (HMV-2, Shimadzu Corp., Japan) on the polished cross-sections of all the rod and flat specimens was performed using a 500 g load, which was applied for 15 seconds. Ten indents were recorded on each of the investigated specimens.

## III. RESULTS AND DISCUSSION

Rod specimens from the EBM-built Alloy 718, shown in Figure 1(a), were extensively characterized in as-built and post-treated conditions. In addition, 5-mm-thick flat specimens were also studied in as-built and post-treated conditions. This was to assess the effects of a given post-treatment on different EBM specimens. Unless stated otherwise, the provided results and discussion are related to the rod specimens shown in Figure 1(a).

### A. As-Built EBM Alloy 718

During EBM production, each layer was melted in two stages. First, the contour was melted to create a frame of the specimens. Later, hatch scanning was employed to consolidate the interior of the sample contained by the contour. The contour region was  $\sim 1.5$  mm wide as observed from Figure 2. Thus, the majority ( $\sim 12$  mm out of 15 mm diameter) of the rod specimen was produced by hatch scanning. The contour and hatch regions exhibited characteristic microstructures as described below. This can be attributed to the differences in melting order, strategy and parameters (such as, beam current, beam speed, spot time) used.

#### 1. Grain structure

*a. Contour* The contour was composed of three passes, numbered as 1, 2 and 3; see Figure 1(b). As shown in Figure 1(b), pass 1 and 2 are the inner contours and pass 3 is the outer contour. Pass 3 also constituted the very perimeter of the specimen cross-sections in each deposited layer. From the SEM investigation of the entire contour, heterogeneous grain morphologies were observed as shown in Figures 2(a) and (b). The outermost part (third contour) exhibited fine equiaxed grains because of the partially molten powder particles that were stuck to the contour region as shown in Figures 2(c) and (d). The adjoining region within the third contour exhibited columnar grains, which appeared to curve and converge towards the centerline of the contour pass when viewed along the

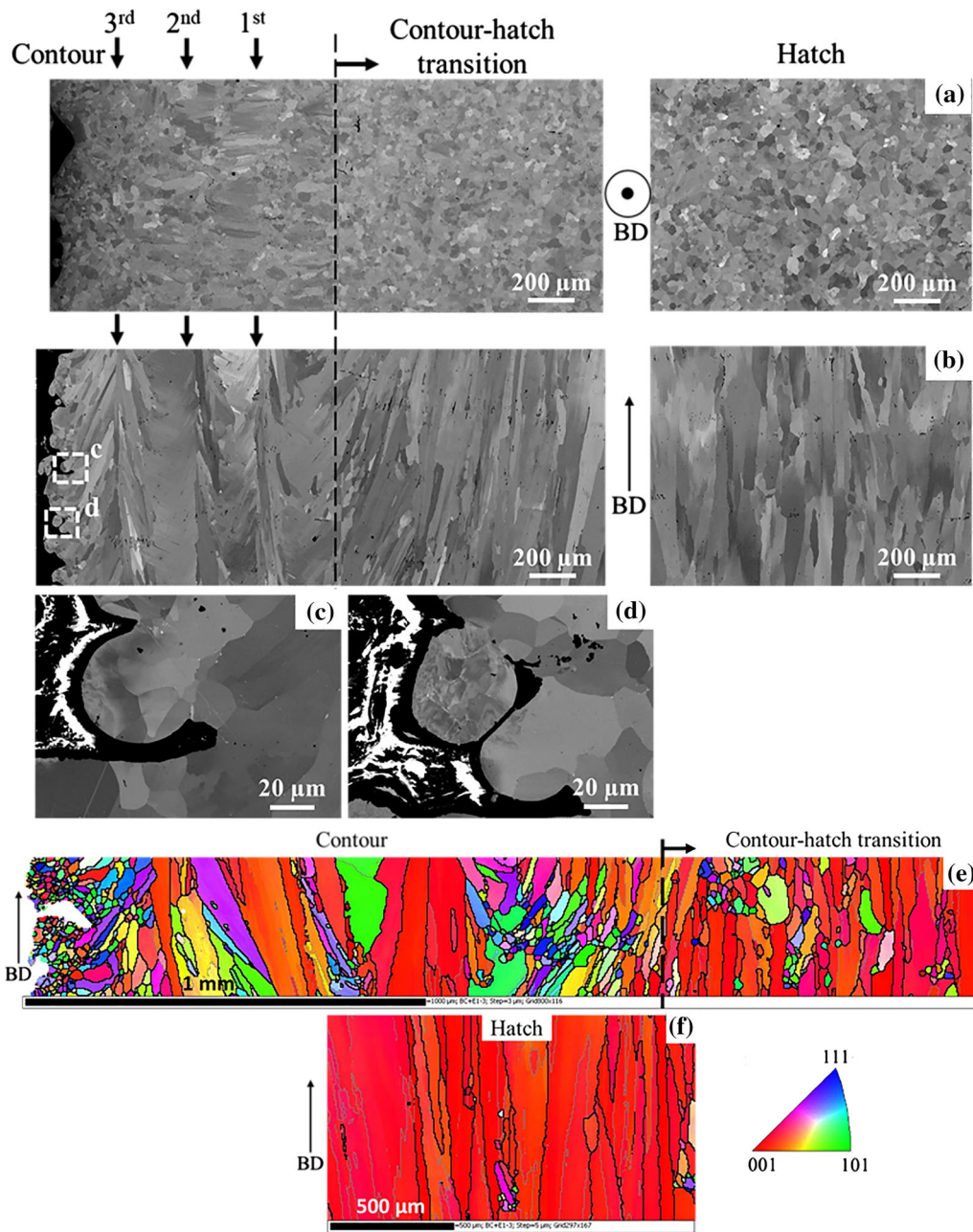


Fig. 2—SEM micrographs revealing the grain structure of the hatch and contour regions in the as-built condition in (a) transverse direction and (b) along the build direction, as marked by the encircled dot and the arrow, respectively; (c) and (d) high-magnification micrographs of the corresponding regions marked in (b). EBSD orientation maps across (e) the contour and contour-hatch transition regions and a larger area scan only in (f) the hatch region are also shown. The maps are presented in inverse pole figure (IPF) coloring with respect to the build direction, and the corresponding color code is provided. The contour melting trajectories (1, 2 and 3) and the onset of the contour-hatch transition region are also specified at appropriate places (Color figure online).

build direction. The overlap regions between the contour passes (3-2 and 2-1) were characterized by the presence of wide columnar grains. The wide columnar grains exhibited lath morphology when observed in the transverse direction as visualized in Figure 2(a). Towards the centerline of contour pass 2 and 1, again slim curved columnar grains were observed. However, the columnar grains in contour pass 1 and the contour-hatch transition region appeared to converge towards the direction of the hatch region. Overall in

the contour region no preferential texture was observed as seen from the EBSD orientation map given in Figure 2(e). Similar observation of heterogeneity in texture and grain morphologies in the contour region and the reason for the same have been widely reported for EBM-built Alloy 718 by Balachandramurthi *et al.*<sup>[30]</sup> as well as for Ti-6Al-4V by Antonyamy *et al.*<sup>[31]</sup> The authors have attributed it to be a result of several factors, *i.e.*, the surrounding powder, shape of the melt pool, epitaxial growth over previously deposited layers

and re-melting of the overlap region between the contour passes. Lastly, it is worth mentioning that the roughness (also contributed by the partially molten powder particles) in the third contour could be improved by changing the processing parameters, such as scanning speed, number of contours, *etc.*<sup>[32]</sup>

*b. Hatch* Unlike the contour region, the hatch was found to be mainly composed of columnar grains with strong texture along  $\langle 100 \rangle$  as can be seen from SEM and EBSD results shown in Figures 2(b) and (f), respectively. This has been widely investigated and was first reported by Strondl *et al.*<sup>[33]</sup> These grains appear to be rather equiaxed when viewed perpendicular to the build direction as seen in Figure 2(a). Therefore, the grains were elongated only along the build direction. The length of the columnar grains was observed to extend up to the order of millimeters as shown in Figure 2(b). This is common for EBM-built Alloy 718 as reported in Reference 21. It is worth mentioning that some stray grains were also observed in the hatch region (Figure 2(f)), which are likely caused by grain nucleation ahead of the solidification front as suggested by Helmer *et al.*<sup>[34]</sup>

## 2. Phase constitution

Both the hatch and contour regions exhibited similar types of phases. The presence of network-like features and globular particles inside the  $\gamma$  matrix was discerned from SEM micrographs given in Figures 3(a) and (b). EDS analysis given in Figure 3(c) shows that the globular particles were rich in Nb and carbon, and depleted of Ni, indicating that the precipitates are NbC carbide. Such primary carbides precipitate during solidification and preferentially form in the interdendritic regions rich in Nb as elaborated by Knorovsky *et al.*<sup>[11]</sup> who also proposed a solidification diagram of Alloy 718. In this context it is worth mentioning that Laves phase forms towards the end of solidification and no Laves phase was observed in the as-built samples as they were extracted from the middle of a tall 100-mm rod. In such an EBM Alloy 718 build, prior work by Kirka *et al.*<sup>[15]</sup> has shown Laves phase to be only present in the top few 100 microns, for explained reasons. It is known and was previously reported by Goel *et al.*,<sup>[24]</sup> through detailed electron microscopic investigation, that NbC can nucleate on TiN particles. Hence, the Ti-peak in the EDS spectrum (Figure 3(c)) may be a result of such a carbide. Ti atoms can also substitute for Nb during formation of carbide as reported for cast Alloy 718.<sup>[13]</sup> However, due to the observed dark core and predominance of Nb inside the carbides, these are referred to as NbC. Sundararaman and Mukhopadhyay<sup>[35]</sup> have reported that the primary carbide phase does not have any particular crystallographic relationship to the  $\gamma$  matrix. Comparing SEM micrographs of the contour and hatch regions, given in Figures 3(a) and (b), respectively, shows that the former exhibited finer carbides. This observation is further supported by the quantitative analysis of the carbides provided in the next section. The size, shape and amount of carbides depend on the local

chemistry and solidification conditions. In case of cast Alloy 718, both Carlson and Radavich<sup>[13]</sup> and Mitchell<sup>[16]</sup> have experimentally observed that an increase in cooling rate (liquid to solid) leads to a decrease in the carbide size. Therefore, the size of carbides could reflect differences in cooling rate in the hatch and contour regions. In this context, it is worth mentioning that by choice of higher cooling rate in the contour region (during simulation) compared to the hatch, Akram *et al.*<sup>[36]</sup> found a better fit between their results from detailed grain simulation analysis and experimental observation. Therefore, the cooling rate in the contour region might have been higher than in the hatch, which could have resulted in the formation of finer carbides in the former.

Higher magnification SEM analysis of both hatch and contour regions revealed that the intragranular network-like features were composed of arrays of needle-like  $\delta$  phase particles, which were stacked parallel to each other as shown in Figure 4. Some dispersed intragranular  $\delta$  phase particles were also observed. However, the  $\delta$  phase particles at intergranular areas were found to be present in isolated form. Although the reason for the observed differences in the arrangement of inter- and intragranular  $\delta$  phase is still elusive, isolated grain boundary particles and clustered arrangement of intragranular  $\delta$  phase have also been previously observed in an Alloy 718 bar by Vanderesse *et al.*<sup>[37]</sup> Intragranular precipitation of  $\delta$  phase is expected to have occurred at the interdendritic areas because of the generally observed tendency to interdendritic segregation of Nb in Alloy 718. Kirka *et al.*<sup>[15]</sup> have reported interdendritic precipitation of  $\delta$  phase in EBM Alloy 718 and attributed it to segregation of Nb in the interdendritic region left after the dissolution of Laves phase. Moreover, with prolonged exposure to high temperature ( $< \sim 900$  °C), Sundararaman *et al.*<sup>[38]</sup> observed intragranular  $\delta$  phase precipitation to be facilitated by the stacking faults within  $\gamma''$  phase. On the other hand, at higher temperatures ( $\sim 900$  °C to  $1000$  °C), the  $\delta$  phase may precipitate directly from the matrix as reported by Sundararaman *et al.*<sup>[39]</sup> In the hatch region of EBM-built Alloy 718, previous studies have reported various kinds of  $\delta$  phase precipitations. In one study by Deng *et al.*,<sup>[21]</sup>  $\delta$  phase was found to be preferentially precipitated at the high-angle grain boundaries. However, spurious precipitation of  $\delta$  phase across the columnar grains in the hatch region has been reported by Kirka *et al.*,<sup>[15]</sup> and Unocic *et al.*<sup>[40]</sup> observed the presence of only intragranular  $\delta$  phases, which were coarser close to the top and finer near the bottom of a 97-mm-tall rod build upright. Nandwana *et al.*<sup>[22]</sup> reported that in EBM-built Alloy 718 produced at lower powder bed temperature ( $\sim 915$  °C) both intragranular and intergranular  $\delta$  phase particles were present; however, the build manufactured at higher temperature ( $\sim 990$  °C) contained only intergranular  $\delta$  phase. Karimi *et al.*<sup>[41]</sup> observed a higher content and longer length of  $\delta$  phase needles in specimens built at a height of 45 mm from the build plate compared to those built on or close (2 mm) to the build plate. On the other hand, when specimens were built on top of each other



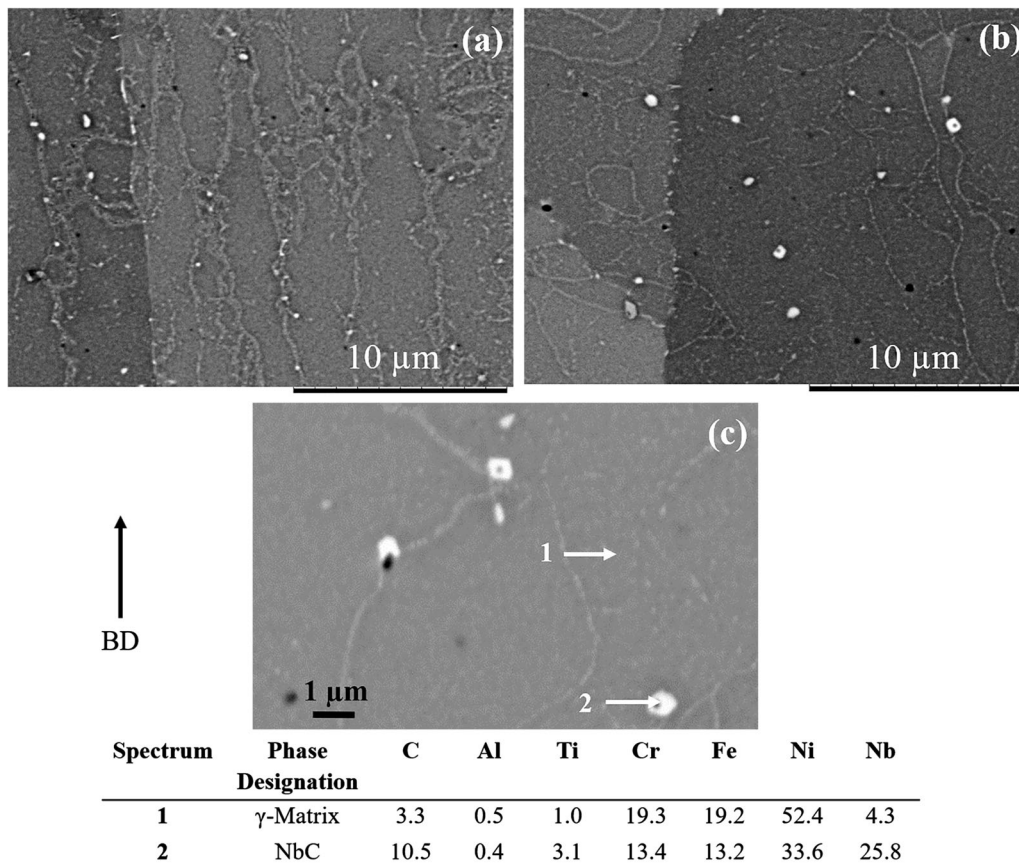


Fig. 3—SEM micrographs showing (a) finer carbide particles in the contour and (b) coarser carbides in the hatch regions in the as-built condition. (c) EDS analysis of a carbide particle and the matrix in the as-built material. The arrow on the left side indicates the build direction.

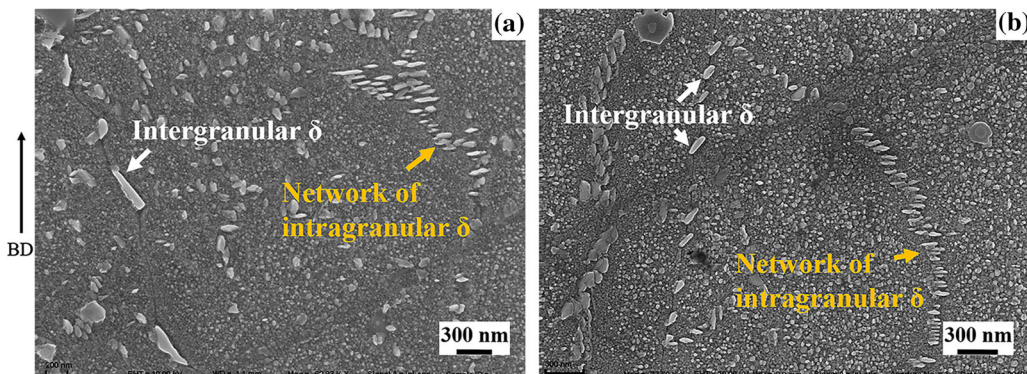


Fig. 4—SEM micrographs of as-built material showing  $\delta$  phase present as isolated and stacked particles at the intergranular and intragranular regions, respectively, in both (a) contour and (b) hatch regions. The arrow on the left side indicates the build direction.

and separated by support structures, Goel *et al.*<sup>[42]</sup> found decreased  $\delta$  phase precipitation with increasing height of the specimens from the build plate. To summarize the above, variation in  $\delta$  phase precipitation can be attributed to the thermal history of the specific build designs. For instance, specimen size,<sup>[40]</sup> build design or height of the sample from the build plate,<sup>[41,42]</sup> type of cooling after manufacturing,<sup>[43]</sup> powder bed preheat temperature,<sup>[22]</sup> *etc.*, can all be influencing factors. A more elaborate explanation was given by Balachandramurthi *et al.*<sup>[44]</sup>

It is pertinent to mention that the  $\delta$  phase particles in both the hatch and contour regions exhibited similar wide variation in size, and no evident difference in the two regions was observed. This can be understood as follows. The  $\delta$  phase forms during solid-state phase transformation after solidification of the molten powder. Although the solidification conditions of the contour and hatch regions were different, as evident from the different grain structure and carbide sizes in the two regions, after consolidation, the hatch and contour region of the specimen might have been exposed to



reasonably similar thermal history inside the heated powder-bed. This similarity in solid-state temperature history of the contour and hatch regions is also reflected in the hardness of the specimens, since Alloy 718 is primarily hardened by the  $\gamma''$  and  $\gamma'$  phases, which are formed during solid-state transformation as previously investigated by Slama *et al.*<sup>[45]</sup> The distribution of  $\gamma''$  and  $\gamma'$  in the  $\gamma$  matrix and the hardness of the hatch and contour regions of the as-built material are discussed later along with the results from the post-treated material to enable easier comparison.

## B. Effect of Post-treatments

### 1. Defects

In the as-built material, the overall defect content in the contour and hatch regions was observed to be  $0.50 \pm 0.3$  pct and  $0.42 \pm 0.2$  pct, respectively (Figure 5(a)). Although the total defect content was similar, the contour seemingly exhibited clustered defects compared to the hatch as shown in Figures 5(b) and (c), respectively. Such clustered arrangement of defects has been previously observed by Karimi *et al.*<sup>[46]</sup> in thin walls of EBM Alloy 718 formed by 1 to 50 layers. Both the post-treatments resulted in a decrease in defect content by an order of magnitude in both the hatch and contour regions as shown in Figure 5(a) and visualized in Figures 5(d) through (g).

### 2. Grain structure

After HIP treatment, abnormal grain growth in both the hatch and contour regions was observed when viewed in transverse direction and along the build direction (Figures 6(a) and (c), respectively). However, for the specimen subjected to HIP + HT, the observed abnormal grain growth was mainly restricted to the contour and contour-hatch transition regions, with the hatch region being largely unaffected as evident from the comparison of Figures 6(b) and (d) with 2(a) and (b). The grain growth is likely caused by the HIP step, which was carried out at 1185 °C. It is also worth mentioning that the strong texture in the hatch region was also largely unaffected by the HIP + HT as shown in Figure 6(f). The observed distinct grain growth behavior after the two HIP treatments could be due to the use of different temperatures (1185 °C and 1200 °C). This finding is in agreement with a previously reported work by Chang *et al.*<sup>[47]</sup> on HIP'ed cast Alloy 718. Though the hatch region exhibited different responses after HIP and HIP + HT, the contour (and surrounding) region, which showed grain growth after both the post-treatments, invariably contained annealing twins. Moreover, fewer (grown) grains with different orientations, compared to the as-built specimen (refer Figure 2(e)), were observed in the contour region as seen from the EBSD orientation map for the HIP + HT specimen shown in Figure 6(e). The abnormal grain growth in the contour region after HIP and HIP + HT is linked to the low density of precipitates, which, if present, can pin the grain boundaries and inhibit their movement. The

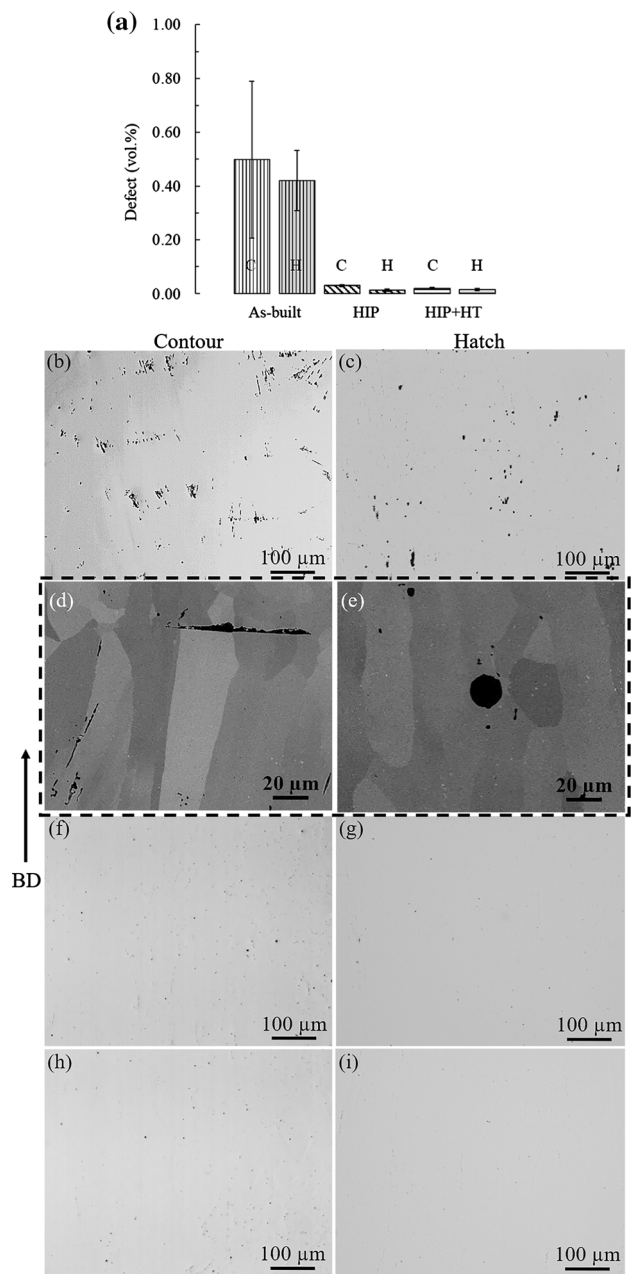


Fig. 5—(a) Defect content in all the rod specimens, where contour and hatch are represented by 'C' and 'H', respectively. Also shown are OM micrographs visualizing defects in the contour and hatch regions of the (b), (c) as-built, (f), (g) HIP and (h), (i) HIP + HT specimen, respectively. (d), (e) Illustrative SEM micrographs (at higher magnification) clearly showing various morphologies of defects present in the as-built condition. The arrow indicates the build direction.

observed heterogeneous distribution of grain boundary pinning  $\delta$  phase could have contributed to the observed abnormal grain growth. In addition, the carbide phase was also heterogeneously present and might have also contributed to the above.<sup>[48]</sup>

The contour region was observed to be more prone to grain growth compared to the hatch region, as noted above for the rod specimens. Therefore, the contour

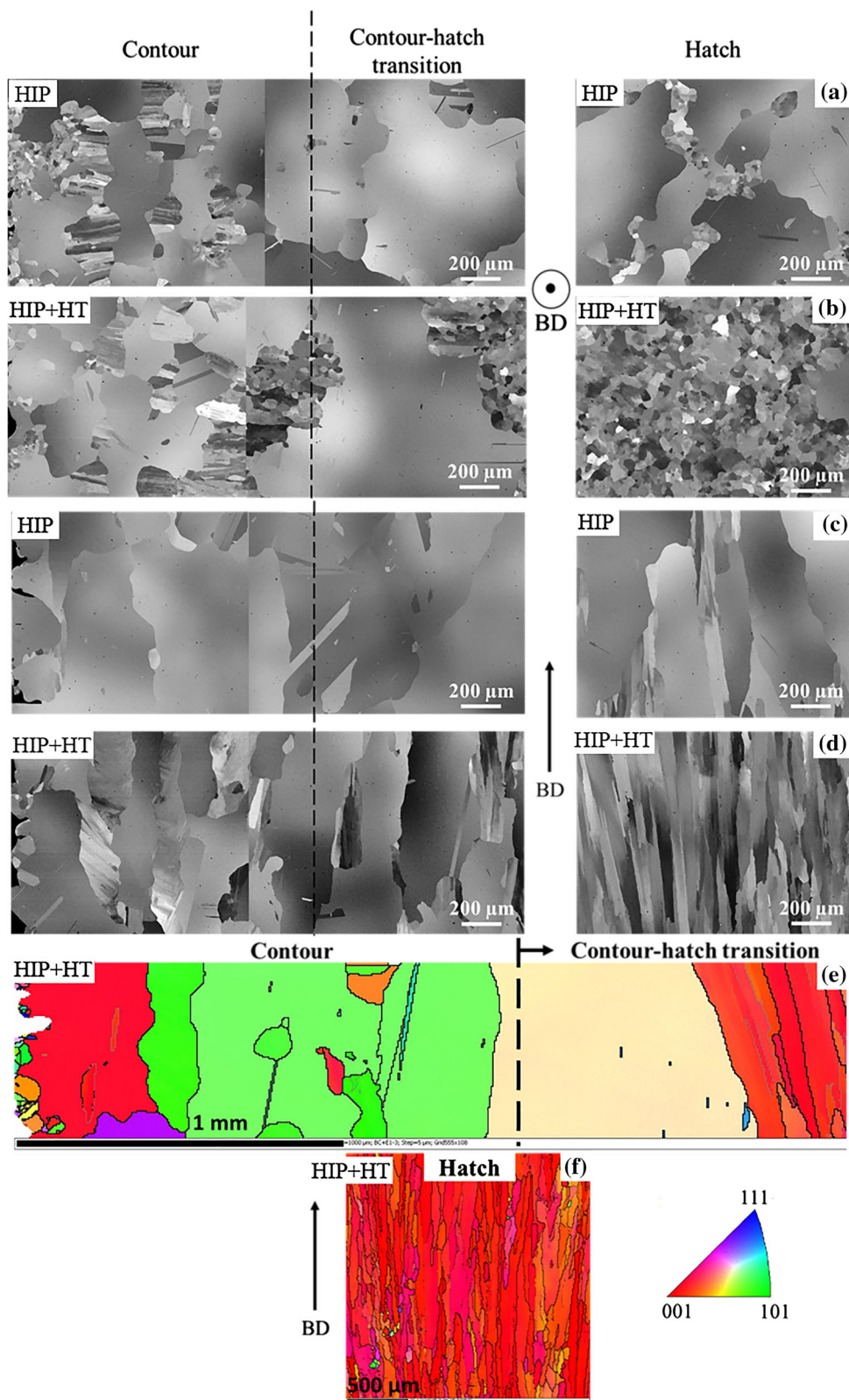


Fig. 6—SEM micrographs of rod specimens showing the grain structure of contour, contour-hatch transition and hatch regions, in transverse direction and along the build direction for the (a), (c) HIP and (b), (d) HIP + HT specimen, respectively. EBSD orientation maps in inverse pole figure (IPF) coloring for the HIP + HT specimen showing (e) extensive grain growth in the contour and contour-hatch transition regions and (f) no significant grain growth in the hatch. The maps are colored with respect to the build direction (indicated by the arrow), and the corresponding color code is provided. For corresponding SEM and EBSD images of the as-built specimen, see Fig. 2 (Color figure online).

region was further examined in another EBM Alloy 718 build comprising flat specimens. After post-treatments (HIP and HIP + HT) these specimens also exhibited significant grain growth in the contour region as shown in Figure 7. Similar to the rod specimens, annealing twins can be seen in the contour region of the flat specimen after the post-treatments. The EBSD data of the flat specimens in as-built, HIP and HIP + HT conditions were further processed to obtain the KAM, GAM and GOS maps. Figure 7 collates the information on misorientation developments in the as-built, HIP and HIP + HT samples. The scans, especially in terms of the inverse pole figure or IPF map (Figure 7(a)), showed a mostly columnar structure in the as-built specimen. HIP or HIP + HT clearly did not alter the grain morphology in the hatch region significantly. In other words, post-treatment of the as-built microstructures did not appear to involve extensive plastic deformation (in the HIP process) and post-deformation (in the HIP + HT) recrystallization and grain coarsening (except in the contour region). Notably the contour region showed grain coarsening, a phenomenon also previously reported during HIP of EBM-built Alloy 718 by Balachandramurthi *et al.*<sup>[30]</sup>

The local misorientation or the KAM distribution (Figure 7(b)) in the as-built specimen was largely restricted to the grain boundaries. This is not unexpected in a solidification structure, an effect of impingement of the solidifying grains as explained by Verlinden *et al.*<sup>[49]</sup> GAM in the as-built specimen was more in the contour region (Figure 7(c)), while GOS (Figure 7(d)) was higher at the center hatch region. GAM represents point-to-point misorientation of a grain, and the average GAM value for a grain thus indicates developments in lattice curvatures (a measure of the overall plastic deformation) in that grain. GOS, on the other hand, indicates point-to-origin or long-range misorientation. Therefore, the GOS is expected to indicate any growth-related lattice curvatures, as generated by the heat flux during solidification. The HIP did spread the KAM distribution from the near grain boundaries to grain interior, while HIP + HT reduced it. The patterns of change in the average numerical values of KAM, GAM and GOS are shown in Figure 7(e). Numerically lower misorientations of the as-built specimen were enhanced by HIP, while HIP + HT brought it back to the original value (clearly through thermal recovery). Figure 7 thus provides a composite picture of misorientation developments in the as-built specimen, but more importantly the misorientations after HIP and HIP + HT.

A closer look to determine the causes of grain growth during post-treatment, and to shed light on the reason for the varied response of the hatch and contour regions of the rod specimens, revealed the following influencing factors: (1) size of grains, (2) orientations of grains, (3) curvature of the grain boundary and (4) Ostwald ripening of carbides. In the as-built material, the contour region had fine columnar and equiaxed grains, with random orientations compared to the relatively strongly textured columnar grains in the hatch region with only few stray grains as previously shown in

Figure 2. Moreover, the grain boundaries in the contour region were curved in more than one plane compared to the hatch region, where the columnar grain boundaries appeared to be curved mainly in the transverse direction. The observed sensitivity for grain growth in the contour region can be attributed to the higher grain boundary curvature. The additional contribution of Ostwald ripening of carbides is described below. It is also worth mentioning that for the HIPed (1200 °C) flat specimen, no evident grain growth was observed in the hatch region. In EBM Alloy 718, Kirka *et al.*<sup>[12]</sup> also observed no grain growth after HIP (1200 °C) in the hatch region, with columnar grain structure, and attributed this to the Zener pinning by carbides present at the grain boundaries. In contrast, in the hatch region with an equiaxed grain structure, they observed grain growth after HIP, which was rationalized by the lack of carbides and precipitates along the grain boundaries. Nandwana *et al.*<sup>[22]</sup> also reported differences in the extent of grain growth during HIP (1200 °C) of two different columnar microstructures depending on the number of grain boundary carbides in the microstructure. Thus, it is evident that the stability of the grains in the hatch region depends on the starting microstructure. Therefore, further investigation is required to determine the reason for the observed differences in response to HIP for the two EBM builds investigated in the present study; see Figures 6 and 7.

### 3. Phase constitution

The carbide particles were retained in the hatch and contour regions of the HIP and HIP + HT rod specimens, as shown in Figure 8. As stated earlier, the contour region contained smaller carbides compared to the hatch region; however, after post-treatment, both the regions appear more comparable in terms of carbide size, which was seen from the results of the quantitative carbide assessment given in Figure 9(a). After post-treatment, the relative increase in larger carbides (> 1 µm in diameter) was much larger in the contour region compared to the hatch. The total NbC content in the two regions was found to be unaffected after post-treatment, as shown in Figure 9(b). The results are indicative of Ostwald ripening of carbides after post-treatment in the contour region, which could have contributed to the observed grain growth. It is important to mention that Seede *et al.*<sup>[50]</sup> found Ostwald ripening of carbides to be associated with grain growth during thermal treatments of LPBF Alloy 718. The grain growth after HIPing at 1160 °C was attributed to the combined effect of Ostwald ripening of carbides and lack of prior particle boundaries. Sames<sup>[51]</sup> reported the growth of large carbides in the hatch region of EBM-built Alloy 718 after heat treatment at 1200 °C. In cast material, Poole *et al.*<sup>[52]</sup> observed an increase in the coarsening of carbides with an increase in temperature for heat treatment in the range of 1150 °C to 1191 °C.

The hatch and contour regions of the as-built material contained  $\delta$  and  $\gamma''/\gamma'$  phases as shown in Figures 10(a) to (c), respectively, with no significant difference in their distribution in the two regions noted. Although HIPing



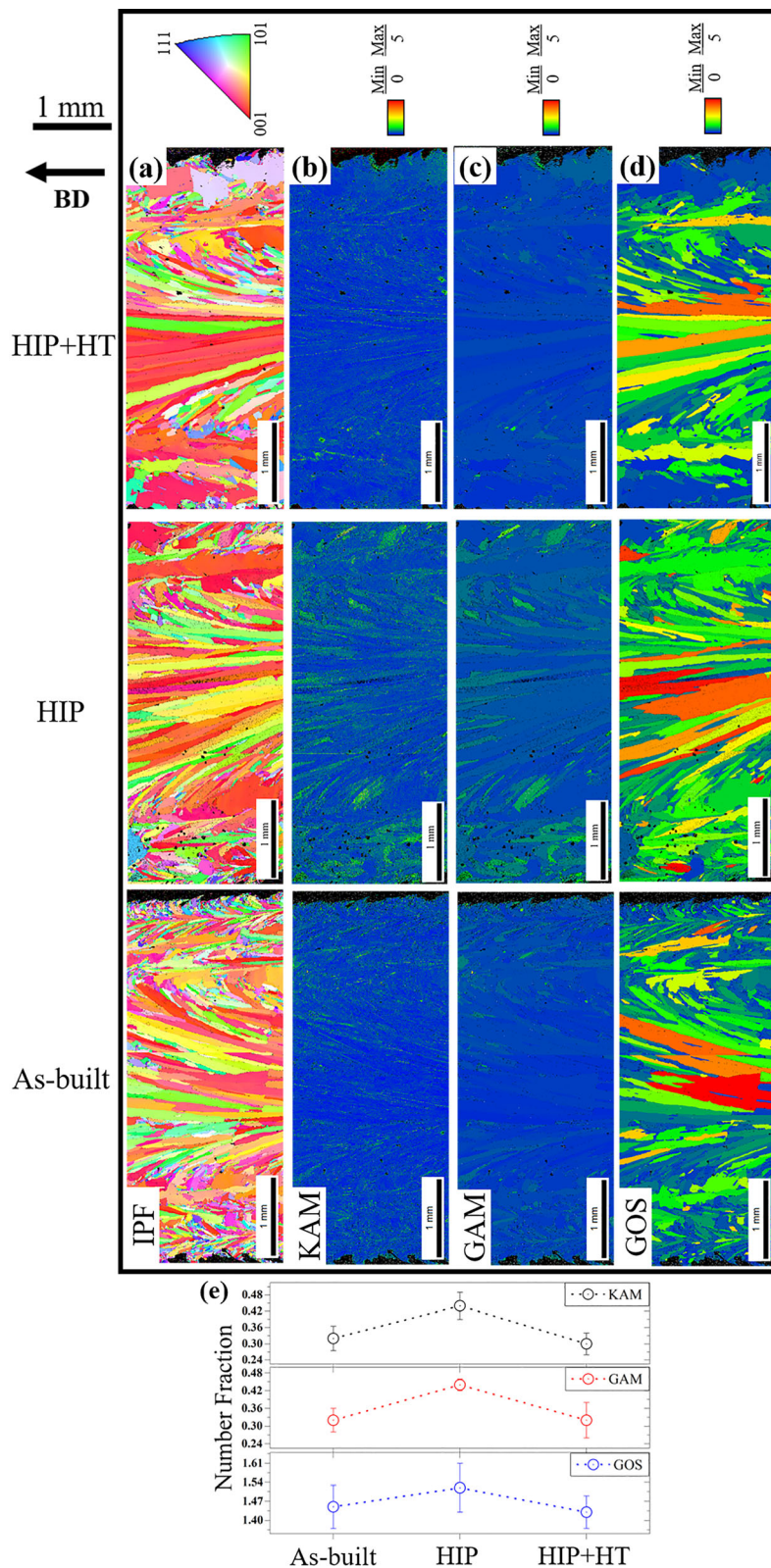


Fig. 7—EBSD scans were taken across the entire width of the 5-mm-thick flat specimen in all three conditions: as-built, HIP and HIP + HT. These are shown as maps of the (a) inverse pole figure (IPF), (b) kernel average misorientation (KAM), (c) grain average misorientation (GAM) and (d) grain orientation spread (GOS). (e) Average KAM, GAM and GOS are also plotted for the respective specimens. The arrow indicates the build direction.

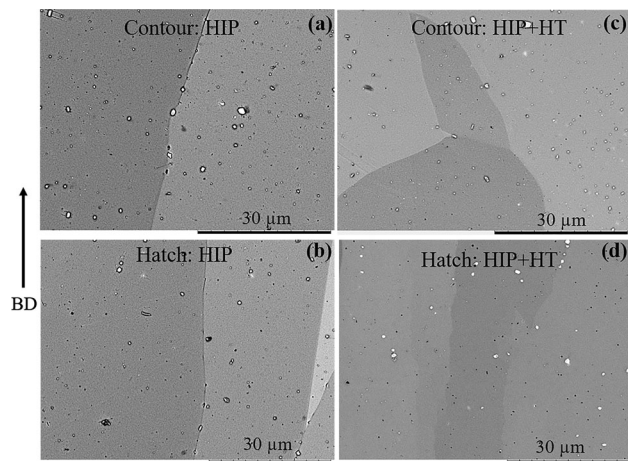


Fig. 8—SEM micrographs of contour and hatch regions in (a), (b) HIP and (c), (d) HIP + HT specimens, respectively. The arrow indicates the build direction.

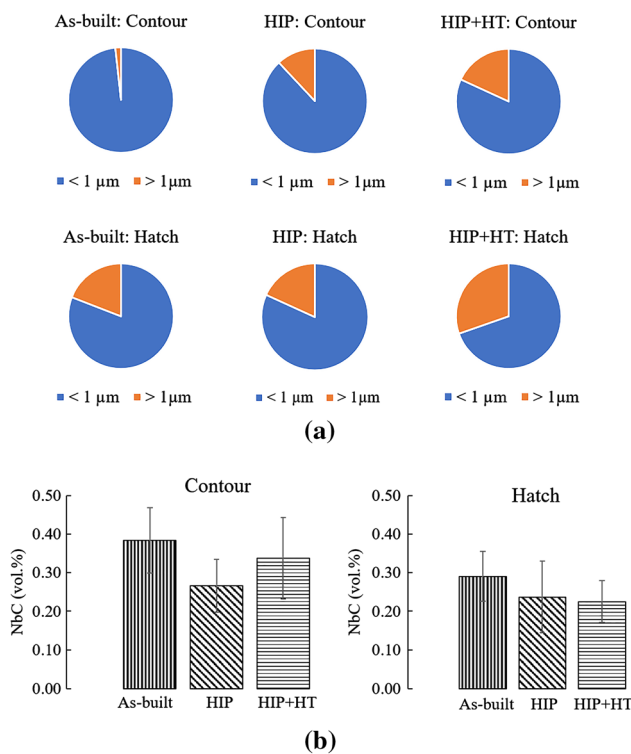


Fig. 9—(a) Pie charts showing the relative number of smaller (< 1 μm) and larger carbides (> 1 μm) in the contour and hatch regions of as-built, HIP and HIP + HT specimens. (b) Quantification of NbC content in the two regions for as-built, HIP and HIP + HT specimens.

resulted in complete dissolution of these phases (Figure 10(d)) because of their lower solvus temperature ( $\delta$ : ~ 1000 °C,  $\gamma''/\gamma'$ : 900 °C/850 °C<sup>[53]</sup>) than the process temperature, after HIP + HT the  $\gamma''/\gamma'$  precipitates were re-precipitated (Figure 10(e)) in both the hatch and contour regions because of the aging step involved in the post-treatment cycle. These microstructural differences were also reflected in the hardness results as described below.

#### 4. Microhardness

The contour and hatch regions exhibited similar microhardness values in transverse and build direction as shown in Figure 11(a). The hardness of age-hardening Alloy 718 is mainly influenced by the amount and size of the strengthening precipitates that hinder dislocation motion. Noting the above, Fisk *et al.*<sup>[54]</sup> also reported a rise in hardness with increase in the size of strengthening precipitates, measured through small-angle X-ray scattering, during early stages of precipitation. The observed similarity in hardness (and microstructure shown in Figures 10(a) and (b)) in the contour and hatch regions and the small standard deviation in the values suggest that the distribution, volume fraction and size of the main strengthening phases  $\gamma''/\gamma'$  are similar in the two regions. During EBM production, the process temperature (~ 1000 °C) is above the solutionizing temperature of  $\gamma''$  (900 °C)/ $\gamma'$  (850 °C); therefore,  $\gamma''/\gamma'$  are expected to precipitate during cooling. From the similar hardness, it can be inferred that the contour and hatch regions of the EBM specimen might have been cooled with similar cooling rates (solid-to-solid) during the precipitation temperature range for  $\gamma''/\gamma'$  as per the time-temperature-transformation diagram of Alloy 718 experimentally developed by Brooks and Bridges.<sup>[55]</sup> After HIP, the hardness dropped to nearly half of the as-built material in both the hatch and contour regions as given in Figure 11(a). This was followed by a regaining of hardness by HIP + HT treatment because of the two-step aging involved. The hardness values after HIP + HT exceed the AMS specification values for precipitation-hardened wrought (346 kgf/mm<sup>2</sup>, AMS 5662) and cast (326 to 427 kgf/mm<sup>2</sup>, AMS 5383) Alloy 718.<sup>[56,57]</sup> The microhardness similarity in the contour and hatch regions of the as-built specimen, decrease after HIP and 'recovery' after HIP + HT were also observed in flat specimens as given in Figure 11(b). This indicates that the hardness was not significantly influenced by the grain size in the present case because after HIP or HIP + HT the grains in the contour region were coarser compared to the hatch. In this context it is worth mentioning that Popovich *et al.*<sup>[58]</sup> found the hardness of heat-treated LPBF-manufactured Alloy 718 to vary with grain size.

#### IV. CONCLUSION

The present study involved a detailed investigation of the microstructure of the hatch and contour regions of EBM-built Alloy 718 in as-built and post-treated conditions comprising HIP and HIP + HT. Both post-treatments resulted in significant densification of the two regions. This was accompanied by grain growth largely in and around the contour region. The grain growth was attributed to the distinct grain size, grain orientations, curvature of grain boundaries and Ostwald ripening of carbides in the contour region compared to the hatch. In the as-built condition, overall the contour region exhibited heterogeneous grain morphologies with no preferred texture, whereas the hatch comprised strongly textured columnar grains. The contour region



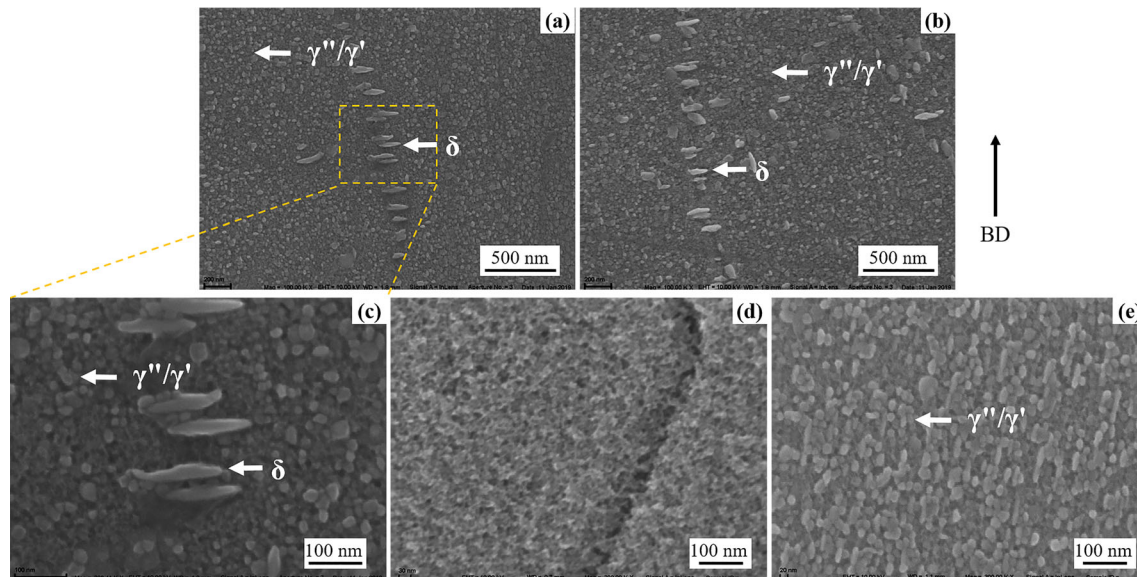


Fig. 10—Higher resolution SEM micrographs showing precipitates ( $\delta$ ,  $\gamma''/\gamma'$ ) in the (a) hatch and (b) contour regions of an as-built specimen. SEM micrographs revealing precipitates present in the hatch region of the (c) as-built and (e) HIP + HT specimen, but absent in the (d) HIP sample. The arrow on the right side indicates the build direction.

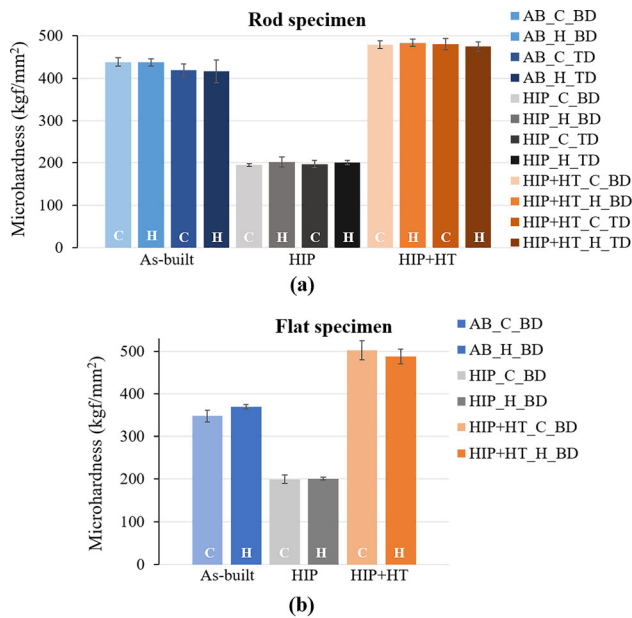


Fig. 11—Microhardness results for all the investigated (a) rod specimens tested in build direction (BD) and transverse direction (TD) and for (b) flat specimens tested along the BD. The abbreviations 'C' and 'H' denote contour and hatch, respectively.

also exhibited greater density of fine carbide particles compared to the hatch. However, after post-treatment (HIP/HIP + HT), the carbide size distribution was found to be relatively similar in the two regions. Post-treatment also resulted in complete dissolution of the  $\delta$  phase. The  $\delta$  phase initially present in the as-built material (in both hatch and contour) was found to exhibit two different arrangements. The intragranular  $\delta$  phase showed a stacked appearance, whereas the

intergranular precipitates were present as isolated particles. Lastly, for both as-built and post-treated specimens, qualitatively no discernible difference in the  $\gamma''/\gamma'$  phase content of the hatch and contour regions was found, which was also reflected in the similar hardness of the two regions. While the  $\gamma''/\gamma'$  content in the HIP + HT specimen was higher than that in the as-built sample, these precipitates were not found in the HIPed material.

## ACKNOWLEDGMENTS

The authors are grateful to Dr. Fouzi Bahbou (Arcam AB, Sweden) for providing the investigated rod specimens. Thanks to Mr. Jonas Olsson (University West, Sweden) for EBM production of flat specimens and to Mr. Magnus Ahlfors (Quintus Technologies AB, Sweden) for carrying out the post-treatments. Kind assistance of Dr. Yiming Yao (Chalmers University of Technology, Sweden) with some of the SEM analysis is also acknowledged. Thanks for the financial assistance go to the KK Foundation (grant no. 20160281) for the SUMAN--Next project, which enabled this study.

## FUNDING

Open access funding provided by University West.

## OPEN ACCESS

This article is licensed under a Creative Commons Attribution 4.0 International License, which permits use, sharing, adaptation, distribution and reproduction



in any medium or format, as long as you give appropriate credit to the original author(s) and the source, provide a link to the Creative Commons licence, and indicate if changes were made. The images or other third party material in this article are included in the article's Creative Commons licence, unless indicated otherwise in a credit line to the material. If material is not included in the article's Creative Commons licence and your intended use is not permitted by statutory regulation or exceeds the permitted use, you will need to obtain permission directly from the copyright holder. To view a copy of this licence, visit <http://creativecommons.org/licenses/by/4.0/>.

## REFERENCES

1. T.J. Horn and O.L.A. Harrysson: *Sci. Prog.*, 2012, vol. 95, pp. 255–82.
2. R.C. Benn and R.P. Salva: in *7th International Symposium on Superalloy 718 and Derivatives*, TMS, Pittsburgh, 2010, pp. 455–69.
3. W.E. Frazier: *J. Mater. Eng. Perform.*, 2014, vol. 23, pp. 1917–28.
4. X. Gong, T. Anderson, and K. Chou: *Manuf. Rev.*, 2014, vol. 1, pp. 1–12.
5. M.M. Attallah, R. Jennings, X. Wang, and L.N. Carter: *MRS Bull.*, 2016, vol. 41, pp. 758–64.
6. S. Goel: Licentiate Thesis, University West, 2019.
7. J. Karlsson, M. Norell, U. Ackelid, H. Engqvist, and J. Lausmaa: *J. Manuf. Process.*, 2015, vol. 17, pp. 120–26.
8. P. Wang, W.J. Sin, M.L.S. Nai, J. Wei, P. Wang, W.J. Sin, M.L.S. Nai, and J. Wei: *Materials (Basel)*, 2017, vol. 10, p. 1121.
9. W.J. Sames, F.A. List, S. Pannala, R.R. Dehoff, and S.S. Babu: *Int. Mater. Rev.*, 2016, vol. 61, pp. 315–60.
10. S. Raghavan, B. Zhang, P. Wang, C.-N. Sun, M.L.S. Nai, T. Li, and J. Wei: *Mater. Manuf. Process.*, 2017, vol. 32, pp. 1588–95.
11. G.A. Knorovsky, M.J. Cieslak, T.J. Headley, A.D. Romig, and W.E. Hammett: *Metall. Trans. A*, 1989, vol. 20A, pp. 2149–58.
12. M.M. Kirka, Y.S. Lee, D.A. Greeley, A. Okello, M.J. Goin, M.T. Pearce, and R.R. Dehoff: *JOM*, 2017, vol. 69, pp. 523–31.
13. R.G. Carlson and J.F. Radavich: *Superalloy 718-Metallurgy and Applications*, The Minerals, Metals & Materials Society, Pittsburgh, 1989, pp. 79–95.
14. D. Zhang, Z. Feng, C. Wang, W. Wang, Z. Liu, and W. Niu: *Mater. Sci. Eng. A*, 2018, vol. 724, pp. 357–67.
15. M.M. Kirka, K.A. Unocic, N. Raghavan, F. Medina, R.R. Dehoff, and S.S. Babu: *JOM*, 2016, vol. 68, pp. 1012–20.
16. A. Mitchell: *Superalloys 718, 625, 706 and Derivatives*, The Minerals, Metals & Materials Society, Pittsburgh, 2005, pp. 299–310.
17. A.D. Patel, J. Erbrick, K. Heck, and G. Maurer: in *Superalloys 2012: 12th International Symposium on Superalloy*, Champion, USA, 2012, pp. 595–600.
18. H. Helmer, A. Bauereiß, R.F. Singer, and C. Körner: *Mater. Sci. Eng. A*, 2016, vol. 668, pp. 180–87.
19. N. Raghavan, R. Dehoff, S. Pannala, S. Simunovic, M. Kirka, J. Turner, N. Carlson, and S.S. Babu: *Acta Mater.*, 2016, vol. 112, pp. 303–14.
20. A.R. Balachandramurthi, J. Olsson, J. Ålgårdh, A. Snis, J. Moverare, and R. Pederson: *Results Mater.*, 2019, vol. 1, p. 100017.
21. D. Deng, J. Moverare, R.L. Peng, and H. Söderberg: *Mater. Sci. Eng. A*, 2017, vol. 693, pp. 151–63.
22. P. Nandwana, M. Kirka, A. Okello, and R. Dehoff: *Mater. Sci. Technol.*, 2018, vol. 34, pp. 612–19.
23. S. Goel, M. Ahlfors, F. Bahbou, and S. Joshi: *J. Mater. Eng. Perform.*, 2019, vol. 28, pp. 673–80.
24. S. Goel, A. Sittiho, I. Charit, U. Klement, and S. Joshi: *Addit. Manuf.*, 2019, vol. 28, pp. 727–37.
25. S. Goel, K. Bourreau, J. Olsson, U. Klement, and S. Joshi: *Materials (Basel)*, 2020, vol. 13, p. 536.
26. S.-H. Chang, S.-C. Lee, T.-P. Tang, and H.-H. Ho: *Mater. Trans.*, 2006, vol. 47, pp. 426–32.
27. W. Tillmann, C. Schaak, J. Nellesen, M. Schaper, M.E. Aydinöz, and K.-P. Hoyer: *Addit. Manuf.*, 2017, vol. 13, pp. 93–102.
28. ASTM E1245-03: *ASTM-International*, <https://doi.org/10.1520/E1245-03R16>.
29. A.J. Schwartz, M. Kumar, B.L. Adams, and D.P. Field: *Electron Backscatter Diffraction in Materials Science*, 2nd ed., Springer, Berlin, 2000.
30. A.R. Balachandramurthi, J. Moverare, N. Dixit, D. Deng, and R. Pederson: *Mater. Charact.*, 2019, vol. 149, pp. 82–94.
31. A.A. Antonysamy, J. Meyer, and P.B. Prangnell: *Mater. Charact.*, 2013, vol. 84, pp. 153–68.
32. C. Schnur: Master Thesis, University West, Sweden, 2017.
33. A. Strondl, R. Fischer, G. Frommeyer, and A. Schneider: *Mater. Sci. Eng. A*, 2008, vol. 480, pp. 138–47.
34. H.E. Helmer, C. Körner, and R.F. Singer: *J. Mater. Res.*, 2014, vol. 29, pp. 1987–96.
35. M. Sundararaman and P. Mukhopadhyay: *High Temp. Mater. Process.*, 1993, vol. 11, pp. 351–68.
36. J. Akram, P. Chalavadi, D. Pal, and B. Stucker: *Addit. Manuf.*, 2018, vol. 21, pp. 255–68.
37. N. Vanderesse, M. Anderson, F. Bridier, and P. Bocher: *J. Microsc.*, 2016, vol. 261, pp. 79–87.
38. M. Sundararaman, P. Mukhopadhyay, and S. Banerjee: *Metall. Trans. A*, 1988, vol. 19A, pp. 453–65.
39. M. Sundararaman, P. Mukhopadhyay, and S. Banerjee: in *Superalloys 718, 625, 706 and Various Derivatives*, Pittsburgh, USA, 1994, pp. 419–40.
40. K.A. Unocic, L.M. Kolbus, R.R. Dehoff, S.N. Dryepondt, and B.A. Pint: *NACE Corrosion*, NACE International, San Antonio, 2014.
41. P. Karimi, E. Sadeghi, D. Deng, H. Gruber, J. Andersson, and P. Nylén: *Int. J. Adv. Manuf. Technol.*, 2018, vol. 99, pp. 2903–13.
42. S. Goel, J. Olsson, M. Ahlfors, U. Klement, and S. Joshi: in *Proceedings of the 9th International Symposium on Superalloy 718 & Derivatives: Energy, Aerospace, and Industrial Applications*, The Minerals, Metals & Materials Series, Pittsburgh, USA, 2018, pp. 115–29.
43. W.J. Sames, K.A. Unocic, R.R. Dehoff, T. Lolla, and S.S. Babu: *J. Mater. Res.*, 2014, vol. 29, pp. 1920–30.
44. A.R. Balachandramurthi, J. Moverare, S. Mahade, and R. Pederson: *Materials (Basel)*, 2018, vol. 12, p. 68.
45. C. Slama, C. Servant, and G. Cizeron: *J. Mater. Res.*, 1997, vol. 12, pp. 2298–16.
46. P. Karimi, E. Sadeghi, P. Åkerfeldt, J. Ålgårdh, and J. Andersson: *Mater. Des.*, 2018, vol. 160, pp. 427–41.
47. S.H. Chang, S.C. Lee, T.P. Tang, and H.H. Ho: *Int. J. Cast Met. Res.*, 2006, vol. 19, pp. 175–80.
48. X. Wang, Z. Huang, B. Cai, N. Zhou, O. Magdysyuk, Y. Gao, S. Srivatsa, L. Tan, and L. Jiang: *Acta Mater.*, 2019, vol. 168, pp. 287–98.
49. B. Verlinden, J. Driver, I. Samajdar, and R.D. Doherty: *Thermo-Mechanical Processing of Metallic Materials*, 11th ed., Elsevier, Oxford, 2007.
50. R. Seede, A. Mostafa, V. Brailovski, M. Jahazi, and M. Medraj: *J. Manuf. Mater. Process.*, 2018, vol. 2, p. 30.
51. W.J. Sames: Ph.D. Thesis, Texas A&M University, 2015.
52. J.M. Poole, K.R. Stultz, and J.M. Manning: *Superalloy 718-Metallurgy and Applications*, The Minerals, Metals & Materials Society, Pittsburgh, 1989, pp. 219–28.
53. S. Azadian: Ph.D. Thesis, Luleå University of Technology, 2004.
54. M. Fisk, J. Andersson, R. du Rietz, S. Haas, and S. Hall: *Mater. Sci. Eng. A*, 2014, vol. 612, pp. 202–07.
55. J.W. Brooks and P.J. Bridges: *Superalloys, Minerals, Metals & Materials Society*, Champion, 1988, pp. 33–42.
56. SAE International: *Aerospace Material Specification, AMS5662*, 2000.
57. SAE International: *Aerospace Material Specification, AMS5383*, 2012.
58. V.A. Popovich, E.V. Borisov, A.A. Popovich, V.S. Sufiarov, D.V. Masaylo, and L. Alzina: *Mater. Des.*, 2017, vol. 131, pp. 12–22.

**Publisher's Note** Springer Nature remains neutral with regard to jurisdictional claims in published maps and institutional affiliations.